

Improvement in the PBF-LB/M processing of the Al-Si-Cu-Mg composition through the use of pre-alloyed powder

*Original*

Improvement in the PBF-LB/M processing of the Al-Si-Cu-Mg composition through the use of pre-alloyed powder / Martucci, A; Gobber, F; Aversa, A; Manfredi, D; Fino, P; Lombardi, M. - In: MATERIALS RESEARCH EXPRESS. - ISSN 2053-1591. - 10:4(2023), pp. 1-18. [10.1088/2053-1591/acc82f]

*Availability:*

This version is available at: 11583/2978889 since: 2023-08-23T13:28:07Z

*Publisher:*

IOP Publishing

*Published*

DOI:10.1088/2053-1591/acc82f

*Terms of use:*

This article is made available under terms and conditions as specified in the corresponding bibliographic description in the repository

*Publisher copyright*

(Article begins on next page)

PAPER • OPEN ACCESS

# Improvement in the PBF-LB/M processing of the Al-Si-Cu-Mg composition through the use of pre-alloyed powder

To cite this article: A Martucci *et al* 2023 *Mater. Res. Express* **10** 046508

View the [article online](#) for updates and enhancements.

## You may also like

- [Parameter optimization and microhardness experiment of AlSi10Mg alloy prepared by selective laser melting](#)  
Xiao Teng, Guixiang Zhang, Jiuping Liang et al.
- [Refinement effect of Zirconium and Samarium on Al-4Mg cast alloy](#)  
K Eisawi, Mahmoud Tash, Waleed Khalifa et al.
- [Effects of Laser-Powder Bed Fusion Process Parameters on the Microstructure and Corrosion Properties of AlSi10Mg Alloy](#)  
Mehran Rafeazad, Parisa Fathi, Mohsen Mohammadi et al.

## Materials Research Express



## PAPER

## OPEN ACCESS

RECEIVED  
28 January 2023

REVISED  
16 March 2023

ACCEPTED FOR PUBLICATION  
28 March 2023

PUBLISHED  
7 April 2023

Original content from this work may be used under the terms of the [Creative Commons Attribution 4.0 licence](#).

Any further distribution of this work must maintain attribution to the author(s) and the title of the work, journal citation and DOI.



# Improvement in the PBF-LB/M processing of the Al-Si-Cu-Mg composition through the use of pre-alloyed powder

A Martucci<sup>1,\*</sup>, F Gobber<sup>1,2</sup>, A Aversa<sup>1,2</sup>, D Manfredi<sup>1,2</sup>, P Fino<sup>1,2</sup> and M Lombardi<sup>1,2</sup>

<sup>1</sup> Department of Applied Science and Technology, Politecnico di Torino, Corso Duca degli Abruzzi 24, 10129 Turin, Italy

<sup>2</sup> Consorzio Interuniversitario Nazionale per la Scienza e Tecnologia dei Materiali (INSTM), Via G. Giusti 9, 50121 Firenze, Italy

\* Author to whom any correspondence should be addressed.

E-mail: [alessandra.martucci@polito.it](mailto:alessandra.martucci@polito.it), [federico.gobber@polito.it](mailto:federico.gobber@polito.it), [alberta.aversa@polito.it](mailto:alberta.aversa@polito.it), [diego.manfredi@polito.it](mailto:diego.manfredi@polito.it), [paolo.fino@polito.it](mailto:paolo.fino@polito.it) and [mariangela.lombardi@polito.it](mailto:mariangela.lombardi@polito.it)

**Keywords:** high-strength al-based compositions, AlSi10Cu4Mg, 4 wt% Cu, gasatomisation, pre-alloyed composition, powder bed fusion, Al-Cu alloys

## Abstract

Among the many additive manufacturing technologies for metals, Powder Bed Fusion-Laser Beam (PBF-LB\ M) stands out for its capacity to produce complex-shaped functional parts. However, the PBF-LB\ M materials portfolio is still limited and the research into new high-performance Al-based alloys is ongoing. The improved properties with the addition of 4 wt% Cu to the AlSi10Mg alloy have been previously investigated in the literature through the *in situ* alloying approach in which the starting powders of Cu and AlSi10Mg are mechanically mixed and directly processed. However, inhomogeneities of alloying elements were found in samples produced with mixed AlSi10Mg+4Cu powders. To overcome this detrimental problem, the use of pre-alloyed AlSi10Cu4Mg powder obtained via gas atomisation process could be a powerful solution. With the aim of demonstrating the beneficial effects of pre-alloyed AlSi10Cu4Mg powders in laser-powder interaction, preliminary SEM investigations were conducted on cross-sectioned SSTs and bulk samples after optimising the process parameters. The deeper microstructural investigations conducted on pre-alloyed AlSi10Cu4Mg samples revealed a higher homogeneity of alloying elements, a smaller cell size of the Al-Si-Cu network (0.5 versus 0.8  $\mu\text{m}$ ) and a slightly smaller mean diameter of equiaxial grains compared to the mixed AlSi10Mg+4Cu ones (6.01 versus 7.34  $\mu\text{m}$ ). In addition, looking closer at the supersaturation level and the precipitation behaviour in pre-alloyed AlSi10Cu4Mg composition, a high solid solution level, a massive presence of  $\text{Al}_2\text{Cu}$  in the cell network and only a few finely dispersed  $\text{Al}_2\text{Cu}$  precipitates within the cells were found. Exploring the benefits of these microstructural features on mechanical properties, an increase in performance of about 18% in micro-hardness tests and more than 10% in tensile and compressive tests were found in the AlSi10Cu4Mg system with respect to the mixed AlSi10Mg+4Cu system. All the thorough investigations proved how using pre-alloyed powders is an important advantage in the PBF-LB/M production of complex Al-based systems.

## 1. Introduction

Metal Additive Manufacturing (AM) provides several advantages with respect to conventional processing and offers unique opportunities for developing new materials and improving their mechanical performances [1]. Powder Bed Fusion-Laser Beam (PBF-LB\ M) is an emerging AM technique in which functional complex-shaped metal components are produced by scanning successive powder layers with a laser source [2, 3]. The cooling rates ( $10^4$ – $10^7$   $\text{K s}^{-1}$ ) achieved during a PBF-LB\ M process are significantly higher than those reached during conventional processing methods (about  $10^2$   $\text{K s}^{-1}$ ), resulting in a finer microstructure and thus in outstanding mechanical properties [4].

The PBF-LB\M technique is promising, but many challenges need to be addressed to exploit its full potential [5]. One of the main problems concerns the low number of metallic systems that can be used to produce defect-free and high-performance components. To date, aluminium alloys have attracted wide interest thanks to their excellent strength-to-weight ratio, but their considerable solidification shrinkage, tendency to oxidation, high laser reflectivity and the poor flowability of their powders make these alloys challenging to process by PBF-LB\M [6–8]. Considering the non-printability by PBF-LB\M of some of the traditional high-strength Al alloys, the challenge of creating new tailored compositions is still ongoing [9, 10].

Among the alloying elements investigated in the literature on Al-based alloys, Cu emerges as the most commonly used. High-strength age-hardenable Al-Cu alloys have attracted strong interest in lightweight applications since their discovery in the 20th century [11–13]. Although Al-Cu alloys are commonly used in traditional processes, PBF-LB/M processing of these alloys only began in 2014 [14]. This is because the wide solidification range and poor fluidity in the molten state of Al-Cu alloys exacerbates the hot cracking susceptibility [14–16]. Zhang *et al* and Nie *et al* demonstrated that the addition of Mg to an Al-Cu binary alloy, together with the use of a markedly low scanning speed, leads to the production of crack-free samples with a good level of densification [17, 18]. In addition, Al-Cu-Mg alloy samples produced by PBF-LB\M have revealed remarkable mechanical properties compared to those obtained by casting (+268% in Yield Strength (YS), +117% in Ultimate Tensile Strength (UTS) and +39% in hardness) [16]. In order to further reduce the hot cracking susceptibility and to improve PBF-LB\M processability, the modification of Al-Cu-Mg alloys with Si has attracted much interest due to the reduction of the solidification range and the improvement of alloy fluidity in the molten state that it produces. Furthermore Al-Si-Cu-Mg alloys permit a significant strengthening effect in as-built conditions, thanks to the solid solution strengthening mechanism and, after heat treatment, thanks to the formation of nano precipitates, which hinder the dislocation movement. Al-Si-Cu-Mg precipitation features (types, sizes and distribution of precipitates) have been thoroughly studied in the literature through the control of the heat treatment in order to maximise the mechanical strengths [19, 20].

One methodology recently explored to obtain Al-Si-Cu-Mg systems for PBF-LB/M technologies is through the addition of Cu to the well-known AlSi10Mg alloy. To the best of the authors' knowledge, these systems have been obtained in three different routes: powder coating [21], powder mixing [22–24] and using pre-alloyed powders [25]. As reported by Garmendia *et al*, coating AlSi10Mg powders with 1 wt% Cu led to promising results in terms of hardness and tensile strengths. However, increasing the percentage of Cu with this methodology is quite complicated and would seriously heighten the laser reflectivity of the powder [21]. Moreover, the complexity of the coating procedure makes it suitable only for producing small batches of powder. This critical aspect can be overcome by the mechanical mixing of AlSi10Mg and pure Cu powders, a quick and effortless method. The mechanical mix of 4 wt% Cu and AlSi10Mg powders was studied in literature resulting in an increase of about 9% in microhardness and about 35% in YS, compared to the pure AlSi10Mg alloy [23]. Despite the promising results obtained with the mechanical mixing method, undesirable clusters of unevenly dissolved Cu were detected [22–24, 26]. The most effective way to obtain these systems without stringent Cu limits and homogenisation problems could be through the use of pre-alloyed powder. Martin *et al* exploited gas atomised powder to build dense and crack-free AlSi10Cu4Mg samples via PBF-LB\M process [25]. In particular, their study was mainly focused on the precipitation behaviour of this composition under heat-treated conditions.

The high potential of AlSi10Mg+Cu compositions has already been demonstrated in the literature. However, the compositions investigated to date have mainly been obtained through complex processes with strong limitations, such as powder coating of AlSi10Mg with pure Cu and methods unable to achieve a proper homogenisation of the alloying elements, such as mechanical mixing of AlSi10Mg and Cu powders. In addition, although Martin *et al* [25] demonstrated the potential of pre-alloyed AlSi10Cu4Mg alloy after direct aging treatment, a systematic study on its as-built condition in terms of microstructural and mechanical properties remains to be conducted. To fill this literature gap, the present work aims to thoroughly evaluate the benefit of using pre-alloyed AlSi10Cu4Mg powder in terms of microstructural features in the as-built condition and the associated mechanical properties with respect to the use of mixed AlSi10Mg+4Cu powders. The AlSi10Cu4Mg powder produced by gas atomisation demonstrated a high level of alloying element homogenisation not observed in the mechanically mixed system. Microstructural analyses were performed to reveal possible differences in Al-Si-Cu network cell sizes and grain sizes in the two systems. To evaluate the effect of using pre-alloyed AlSi10Cu4Mg powder on the solid solution and precipitation levels, x-ray Diffraction (XRD), Differential Scanning Calorimetry (DSC) and Electron Backscatter Diffraction (EBSD) were performed. Finally, the effects of pre-alloyed AlSi10Cu4Mg composition on the mechanical behaviour of PBF-LB/M samples were studied by tracing its microhardness profile and analysing the tensile and compressive properties.

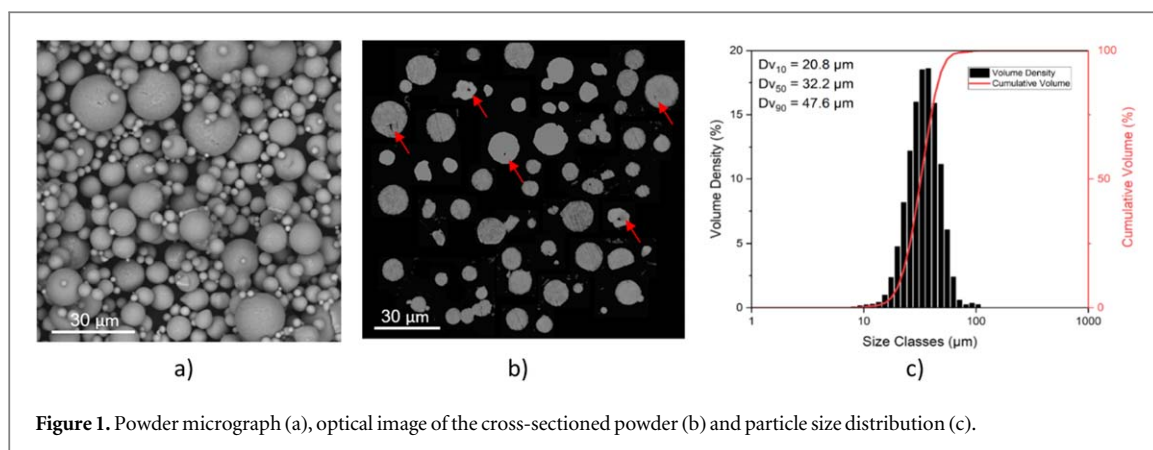


**Figure 1.** Powder micrograph (a), optical image of the cross-sectioned powder (b) and particle size distribution (c).

## 2. Material and methods

### 2.1. Powder characterisation

To study the effects of powder pre-alloying in PBF-LB/M process, AlSi10Cu4Mg powder was produced by our research group using PSI's HERMIGA 100/10 VI gas atomiser starting from AlSi10Mg and pure Cu ingots. A backfill operation was carried out before the vacuum induction melting to avoid the evaporation of volatile elements. In order to avoid oxidation issues, an inert high purity argon atmosphere was used during the whole gas atomisation process. In addition, due to the high reactivity of the powder, after gas atomisation, a passivation step was carried out to prevent explosivity problems. In order to observe the morphology of powder particles a Scanning Electron Microscopy (SEM) analysis was carried out using a Phenom XL. As can be observed in figure 1(a), all particles have a spherical shape that meets the requirements of the PBF-LB\M production. Only a limited number of satellites was found, probably due to the ultrafine powder fraction. The cross-sectioned particles revealed limited and small internal gas porosities (indicated with red arrows in figure 1(b)) resulting from the gas atomisation process. After an accurate image analysis on 20 images taken with the optical microscope (Leica DMI 5000 M), the internal porosity of the particles was calculated to be around 0.01%. The size range of powder in the as-produced condition was 8-105 μm, as measured using a Mastersizer3000 laser diffraction particle size analyser. In particular, as reported in figure 1(c), the particles were characterised by D10, D50 and D90 values of 20.8, 32.2 and 47.6 μm, respectively. Prior to the PBF-LB\M production, the powder was sieved between 20 and 50 μm as suggested by Concept Laser and dried to remove surface moisture from particles.

The powder characterisation was then concluded with XRD analysis and subsequent phase identification (figure 2). This characterisation is essential in order to verify that all pure copper reacted with the AlSi10Mg during gas atomisation. The absence of Cu peaks in the XRD spectrum confirms that, thanks to the rapid solidification involved in the gas atomisation process, the Cu is in solid solution or reacts with Al to form the Al<sub>2</sub>Cu phase.

### 2.2. PBF-LB\M production

The entire PBF-LB\M production was performed using a Concept Laser Mlab cusing R. This system features a build volume of 90 × 90 × 80 mm<sup>3</sup> and a fiber laser with a maximum power of 100 W, a wavelength of 1070 nm and a laser spot of 50 μm. To quickly achieve Power (P) and scan speed (v) values suitable for the bulk production with a limited powder waste, the Single Scan Tracks (SSTs) method was used. This method has been widely applied in the literature for a preliminary tuning of P and v [27, 28]. In addition, an innovative algorithm implemented in a previous author's work [29] was used to quickly discharge parameters unsuitable for the bulk production. This algorithm is able to identify the most suitable P-v combinations by discarding the non-continuous scans and considering the SSTs quality. This powerful tool was exploited by analysing a wide range of power and scan speed values ( $P = 80 - 95 \text{ W}$  and  $v = 300 - 1400 \text{ mm s}^{-1}$ ), resulting in a Linear Energy Density (LED) range from 0.09 to 0.14 Jmm<sup>-1</sup> applying equation (1).

$$LED = \frac{P}{v} \quad (1)$$

The P and v sets resulted from the software analysis and used for the bulk production were reported in table 1. According to the methodology implemented by Bosio *et al*, hatch distance (hd) values were set for each P and v combination considering the mean SST width and an overlapping of 0% between nearby tracks [30]. Moreover, following the standard indications for Al-based alloys processed with the Concept Laser Mlab cusing R machine,

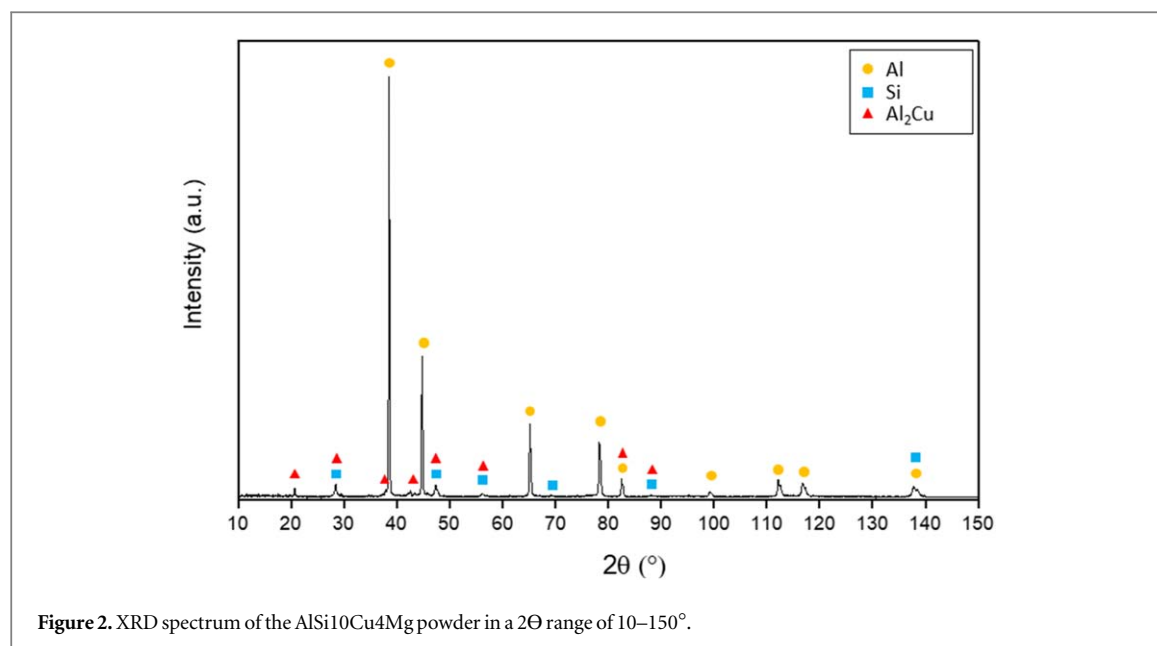


Figure 2. XRD spectrum of the AlSi10Cu4Mg powder in a  $2\theta$  range of 10–150°.

Table 1. Parameters used for the PBF-LB\M bulk production.

Power (W)	Scan speed ( $\text{mm s}^{-1}$ )	Hatch distance ( $\mu\text{m}$ )	Layer thickness ( $\mu\text{m}$ )	VED ( $\text{J mm}^{-3}$ )
90	650	97	15	95
90	800	92	15	81
95	800	85	15	93
95	950	80	15	83

a layer thickness ( $l$ ) of 15  $\mu\text{m}$  was set, resulting in a Volumetric Energy Density (VED) range from 81 to 95  $\text{J mm}^{-3}$  applying equation (2).

$$VED = \frac{P}{l \cdot hd \cdot v} \quad (2)$$

All the parameters used for the bulk production are summarised in table 1.

After finding the parameters related to an optimal densification level, a second PBF-LB\M job was performed to produce specimens for more in-depth characterisations. The job included cubic samples 10 × 10 × 10  $\text{mm}^3$  for microstructural and microhardness evaluation, flat tensile specimens for the tensile properties investigation and cylindrical samples for the compressive test. The flat tensile samples were designed according to ASTM E8 standard, produced with a thickness of 4 mm along the building direction, and rotated by 45° on the platform. The cylindrical samples were designed according to ASTM E9 standard with a diameter of 6.5 mm and a height (along the build direction) of 12.5 mm. A width to length ratio of 1:2 is usually recommended to ensure that no buckling occurs. The orientation of the samples on the build platform was chosen to avoid the need for additional machining or the use of supports.

## 2.3. Characterisations

### 2.3.1. Investigation of microstructural features

To observe the laser-powder interactions and verify a homogeneous diffusion of the alloying elements, the first step was an optical analysis through Phenom XL SEM, equipped with a Back-Scattered Electron (BSE) detector of the SST cross sections. Subsequently, bulk samples were produced with the parameters resulting from the on-top analysis of the SSTs. The as-built bulk specimens were removed from the platform using an electrical discharge machine as the first step. To evaluate the densification level, all samples were cut along the building direction and polished using the standard metallographic procedure. A Leica DMI 5000 M optical microscope was used to take 10 micrographs (100x magnification) for each building condition. Subsequently, these micrographs were processed using ImageJ software, which is able to distinguish the pores from the matrix after



thresholding and thus calculate the relative density averaged over the 20 measures. After identifying the process conditions to ensure the highest level of densification, further microstructural characterisations were carried out. The copper homogenisation level was examined in a Phenom XL SEM, equipped with a BSE detector. In order to deeply observe the Al/Si/Al<sub>2</sub>Cu network, advanced microstructural investigations were performed through a Field Emission Scanning Electron Microscopy (FESEM) analysis using a Tescan S9000G FESEM equipped with an BSE detector and a Energy Dispersive x-ray (EDX) analysis with a Phenom XL SEM. Grain morphology and orientation were investigated through an EBSD analysis performed with Tescan S9000G FESEM. EBSD orientation maps were recorded at 500 X and 5 k X magnification and a step size of 1.1 and 0.11  $\mu\text{m}$  respectively. The SEM was operating at 20 kV, and 10 nA and the samples were tilted 70° and with a working distance of 8 mm.

### 2.3.2. Phase identification and thermal analysis

A PANalytical X-Pert diffractometer was used for the phase identification. The XRD analyses were performed on the XZ plane at 40 kV and 40 mA in a Bragg Brentano configuration, using a Cu K $\alpha$  radiation. The phase identification procedure was performed on the basis of the following reference patterns: Star 00-004-0787 for Al, Calculated 01-089-1980 for Al<sub>2</sub>Cu and Calculated 01-077-2109 for Si. The lattice parameter of face centred cubic (fcc) Al was calculated with the  $\cos\theta \cot\theta$  method. In order to perform a quantitative evaluation of the supersaturation condition of the Al matrix, Vegard's law was exploited using the lattice parameter of the PBF-LB\M sample and the near-equilibrium one. A reference value for near-equilibrium behaviour was obtained by analysing a sample subjected to melting and subsequent very slow cooling in order to achieve a near-equilibrium microstructure. The reaction sequence was determined through a DSC analysis with the NETZSCH DSC 214 Polyma instrument. The DSC test was conducted on the as-built sample with a weight of approximately 68 mg. The heating rate was fixed at 10 °C min<sup>-1</sup> and the temperature was varied in the range 20 °C-450 °C. The thermal analysis was carried out with an Al<sub>2</sub>O<sub>3</sub> crucible and a protective argon atmosphere.

### 2.3.3. Mechanical tests

The mechanical performances were investigated through Vickers microhardness, tensile and compression tests. The microhardness testing was conducted using a Vickers tester VMHT according to ASTM E384 standard. Ten microhardness indentations were performed on the XZ plane using a static load of 0.5 kg and a dwell time of 10 s. The tensile tests were carried out at room temperature according to ASTM E8 standard, using a Zwick/Roell ProLine Z050 universal tensile test machine and applying a strain rate of  $8 \times 10^{-3} \text{ s}^{-1}$ . The strain was measured by a strain gauge with an initial length of 10 mm. In order to calculate the deformation values from specimen regions subjected only to uniaxial stress, the strain gauge was positioned at the middle of the gauge length. To obtain an accurate evaluation of tensile properties, three samples were tested. Subsequently, in order to investigate the possible fracture causes of the specimens subjected to tensile loading, the fracture surfaces were observed by a Tescan S9000G FESEM equipped with an BSE detector. Finally, compression tests of as-built samples were also performed on a Zwick Z100 machine with a constant strain rate of  $3.3 \times 10^{-4} \text{ s}^{-1}$  according to the ASTM E9 standard. Three tests were conducted in order to accurately evaluate compressive properties.

## 3. Results and discussion

### 3.1. Laser-powder interaction study with Single Scan Tracks

A time- and effort-saving method to evaluate the influence of different powder production techniques on the laser-powder interaction phenomena could be through the use of SST. The SST corresponds to a laser track scanned on a single powder layer previously spread onto a substrate. As already studied for the mixed AlSi10Mg+4Cu powders, SSTs were produced with the pre-alloyed AlSi10Cu4Mg powder and different LED values. Through an SEM investigation with the BSE detector of the SST cross-section, a preliminary evaluation of the alloying element homogeneity could be obtained. In fact, the BSE detector identifies the highest atomic weight elements and observes their diffusion in the matrix. Comparing the SEM analysis conducted on SSTs cross-sections realised with the mixed AlSi10Mg+4Cu system or the pre-alloyed AlSi10Cu4Mg powder, two completely different scenarios could be observed (figure 3). The AlSi10Cu4Mg SSTs revealed the absence of Cu segregation and a homogeneous Cu distribution already after the single laser scan realised in the SST production (figure 3(a)). In contrast, the AlSi10Mg+4Cu SSTs did not show the same homogeneity as the pre-alloyed composition, revealing unfused Cu particles, Cu-rich bands following the Marangoni flow and a general irregular Cu distribution (figure 3(b)) [26].

The presence of pure copper in the mixed AlSi10Mg+4Cu system is an adverse condition for a proper laser-powder interaction due to the extremely different thermal conductivity and melting temperature of the starting powders [31, 32]. On the other hand, observing the XRD spectrum performed on pre-alloyed AlSi10Cu4Mg

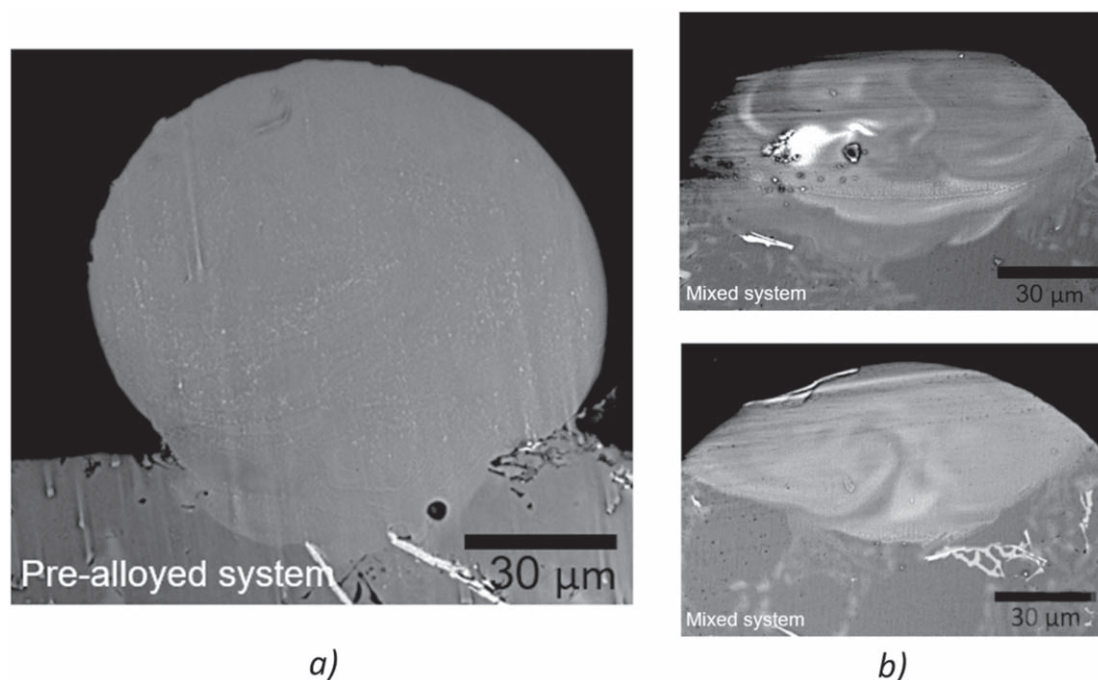


**Figure 3.** A representative BSE micrograph of the SST cross-section obtained with the pre-alloyed system (a) studied in the present work and BSE micrographs obtained with the mechanically mixed system (b). Adapted from [26], Copyright (2022), with permission from Elsevier.

powder (figure 2), no peaks referring to the Cu pattern were visible, but only peaks of  $\text{Al}_2\text{Cu}$  phase. The complete absence of Cu peaks reveals that during the rapid solidification of the gas atomisation process the entire amount of Cu completely diffused and partially reacted with the Al to form the  $\text{Al}_2\text{Cu}$  phase. Notwithstanding the intermetallic presence in the pre-alloyed  $\text{AlSi10Cu4Mg}$  powder, a homogenous diffusion of the alloying elements took place during laser scanning. Probably this occurred because, as observed in the literature, the dissolution of the Al-Cu phases takes place at temperatures close to  $480^\circ\text{C}$ , significantly below the temperature needed for the pure copper [33]. The homogenous condition achieved after just a single laser scan is a key strength of using pre-alloyed powders.

The SST method gives also information on the preliminary tuning of the process parameters for bulk production. In the present study, a wide range of P-v combinations was explored and reported in figure 4. The parameters not able to guarantee adequate bulk densification were rapidly discarded on the basis of on-top SST morphologies [29]. In particular, in figure 4, the conditions in which SSTs with strong discontinuities were obtained are marked in red and the conditions with low-quality indexes are indicated in orange.

Exploiting the P-v information provided by the software, Concept Laser indications for layer thickness suitable for Al-based alloys, and setting hd values calculated on the basis of the SSTs width under the same P-v conditions, bulk samples of the pre-alloyed composition were processed via PBF-LB/M.

### 3.2. Bulk processability

In figure 5(a), the relative density values of the bulk PBF-LB/M samples were plotted against the VED values, and an increasing trend is clearly evident. In addition, to clarify the effect of power and scan speed values on the densification behaviour, one micrograph for each process condition was reported in figure 5(b).

No cracks were found in all process conditions and a mean density of 98.8% was recorded for the samples produced with the highest VED ( $95\text{ Jmm}^{-3}$ ). The latter were processed at 90 W as laser power and  $650\text{ mms}^{-1}$  as laser scan speed and were characterised only by spherical and small-sized pores, also known as gas porosity. The origins of these porosities can be many, including the moisture on the powder surface, the gas trapped in the particles after gas atomisation and the dynamics of the PBF-LB/M process. As demonstrated by Weingarten *et al* [34], gas porosities can be drastically reduced through an efficient drying of the powder by removing surface moisture from particles. Based on this study, in order to avoid pore formation, the  $\text{AlSi10Cu4Mg}$  were dried immediately before the PBF-LB/M process. Moreover, gas-trapped particles can be reduced by optimising the gas atomisation process. Instead, although gas atomisation is the most advantageous process for the production of powders with controlled particle size, few satellites and spherical shape, the phenomenon of trapped gas within the particles cannot be completely eliminated. Calculating the internal porosity of the powders



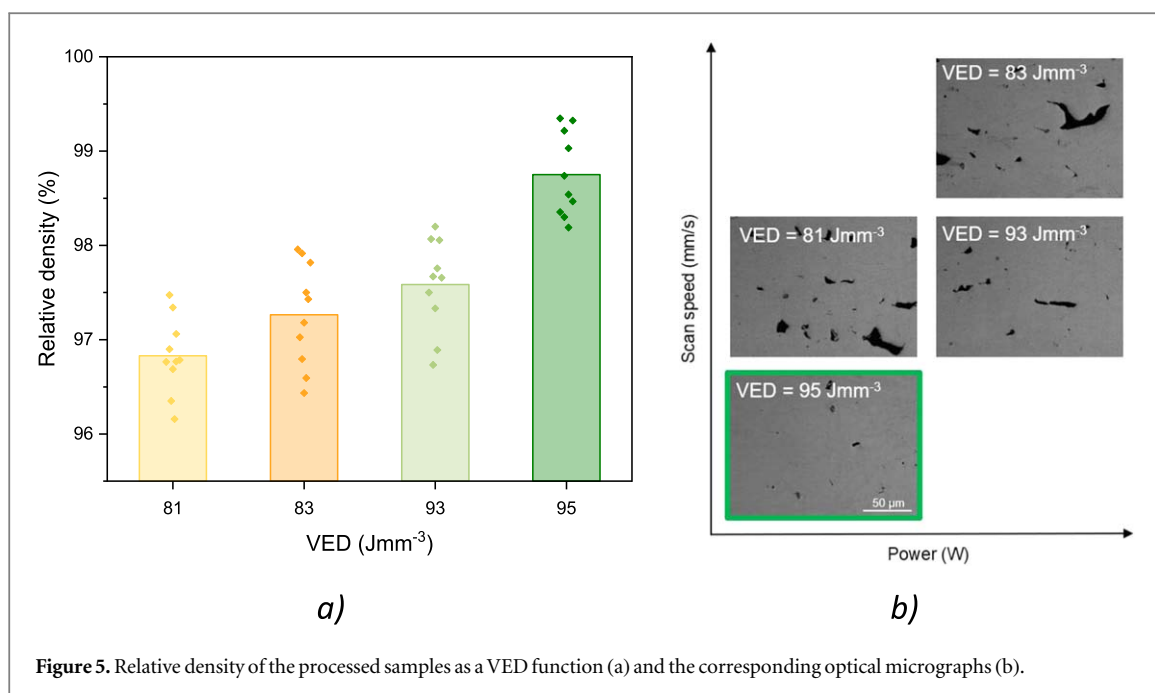
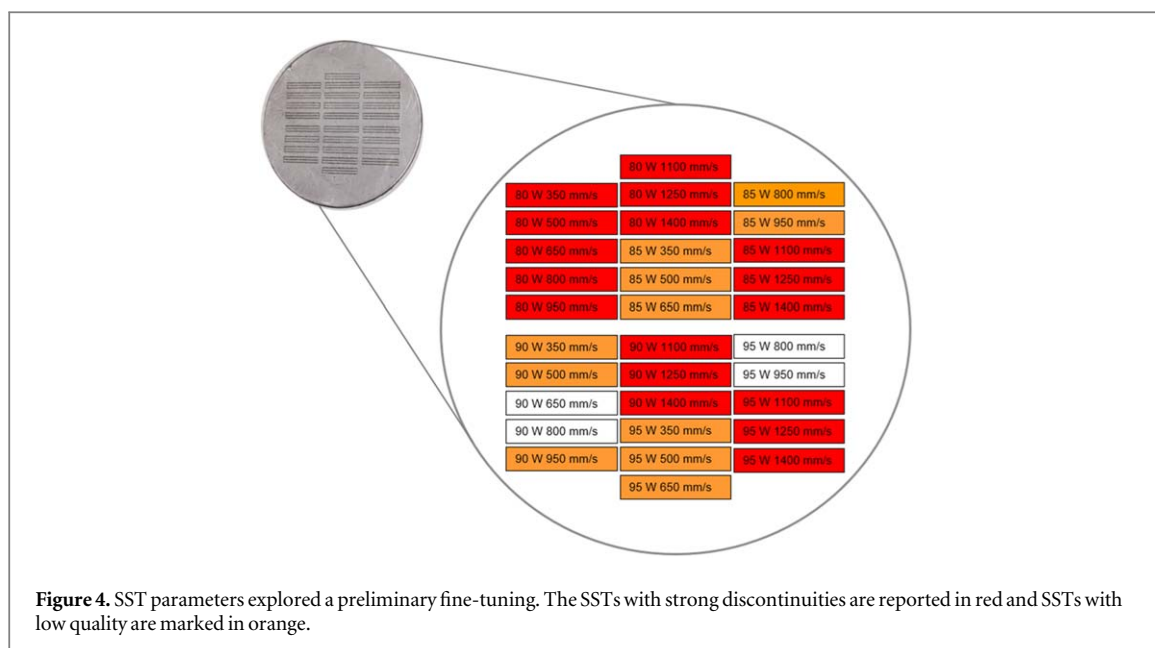


(figure 1(b)), only 0.01% porosity was found. This suggests that the porosity found in the bulk samples cannot be attributed to the gas atomisation process. Another aspect to be taken into account is that the PBF-LB\ M process takes place in an inert atmosphere and the powder stream can trap the protective gas (argon). The latter enters the melt pool through the Marangoni's flow, which tends to retain entrapped gas bubbles. Notwithstanding, considering the low porosity and the geometrical features of this type of porosity, they should not be considered detrimental to mechanical performance. On the other hand, figure 5(b) show as the presence of non-spherical pores with irregular shapes and larger sizes increased with the scan speed values. In the literature, these porosities are known as lack of fusion pores and are attributed to an insufficient energy input that usually occurs when too high scan speed or low VED values are used [31]. The highly irregular shape of these porosities leads to a notch effect, reducing the loading capacity and thus compromising the mechanical performance. Based on these considerations, the parameters highlighted in green in figure 5(b) were selected.

### 3.3. Microstructural characterisations

After identifying the proper process conditions, an SEM investigation with a BSE detector was performed on cross-sectioned bulk AlSi10Cu4Mg samples in order to verify the effectiveness of the use of pre-alloyed powder

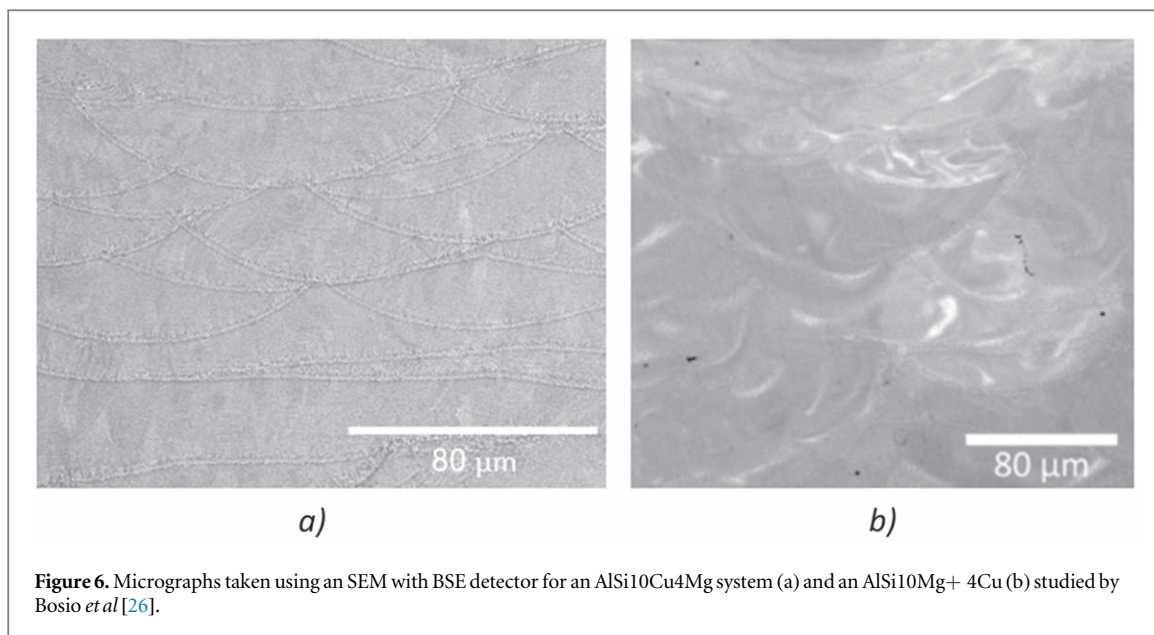


**Figure 6.** Micrographs taken using an SEM with BSE detector for an AlSi10Cu4Mg system (a) and an AlSi10Mg+ 4Cu (b) studied by Bosio *et al* [26].

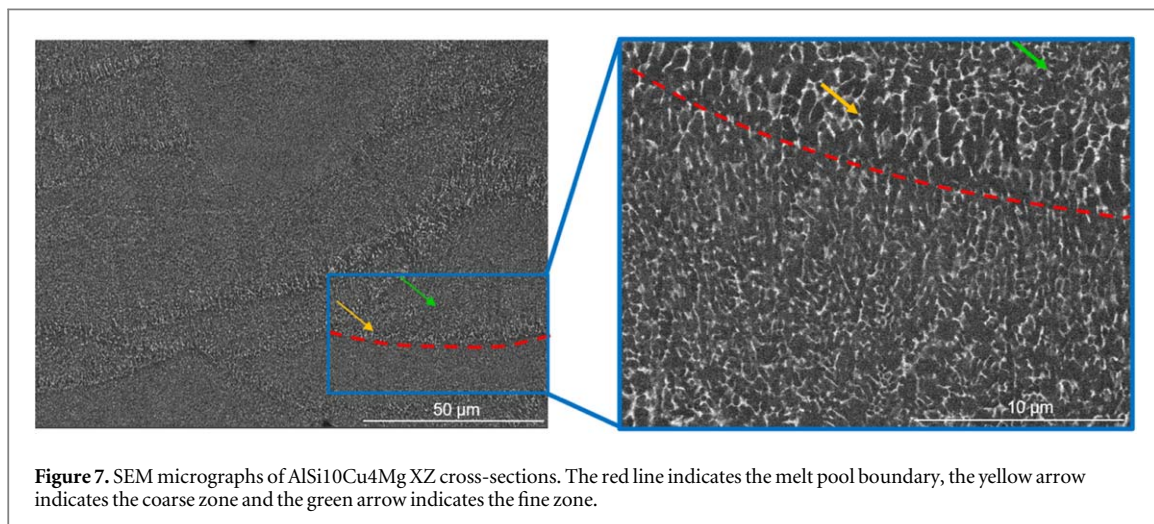


**Figure 7.** SEM micrographs of AlSi10Cu4Mg XZ cross-sections. The red line indicates the melt pool boundary, the yellow arrow indicates the coarse zone and the green arrow indicates the fine zone.

in achieving a good level of homogenisation of alloy elements when multiple laser scans are involved (figure 6). The results were promising, in fact, the homogeneous distribution of alloying elements found in cross-sectioned SSTs was confirmed by optical analysis of the cross-sectioned bulk samples and Cu-enrich phases seem to be located uniformly in the Al-Si network (figure 6(a)). On the contrary, despite the successive scans and the different thermal history involved in bulk production, the AlSi10Mg+4Cu bulk samples characterised by Bosio *et al* did not exhibit an improvement over what was observed with single scans, revealing a locally inhomogeneous Cu distribution (figure 6(b)) [26]. In fact, in AlSi10Mg+4Cu bulk samples a VED of  $40 \text{ Jmm}^{-3}$  and a building platform heated at  $100^\circ\text{C}$  allowed a good densification level but they were not able to yield the complete Cu diffusion.

In order to better investigate microstructural features of the pre-alloyed AlSi10Cu4Mg, a more detailed SEM, FESEM and EBSD analyses were conducted. The SEM investigation of xz plane (perpendicular to the build direction) led to the identification of three melt pool areas with different network morphologies (figure 7): an altered area at the melt pool boundary (indicated with a red line) with a very fine and partially broken network, the coarse zone contiguous to the melt pool boundary (indicated with a yellow arrow) with coarser cells and thickened network walls and the fine area in the central zone of the melt pool (highlighted with a green arrow) with smaller cells and thinner network walls. Probably the altered area results from the fine zone of the previous layer affected by heat during the deposition of the new layer.

The microstructure heterogeneity observed in the melt pool of AlSi10Cu4Mg bulk samples is similar to the one observed in AlSi10Mg [35–38] and in locally homogeneous areas of the mixed AlSi10Mg+4Cu system [26]. In addition, in the central zone of the melt pool, FESEM investigation using Secondary Electron (SE) and BSE

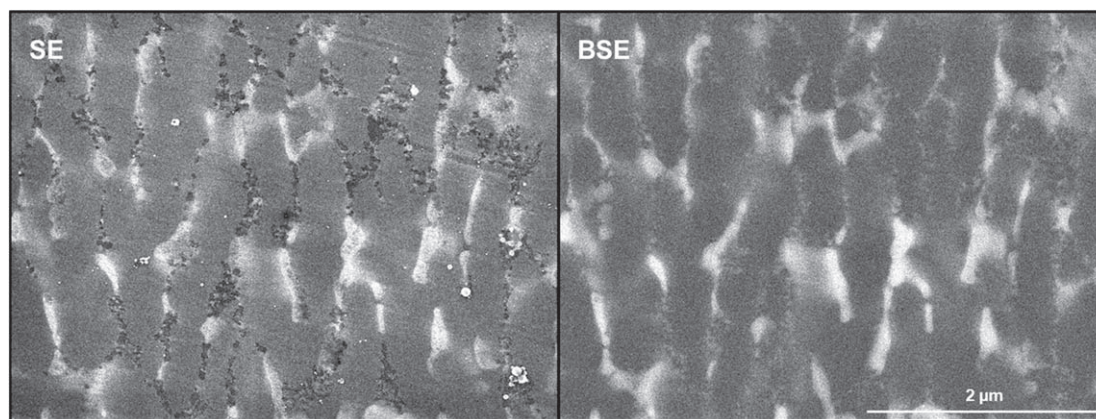


**Figure 8.** FESEM micrographs of an AlSi10Cu4Mg XZ cross section in dual mode: SE and BSE.

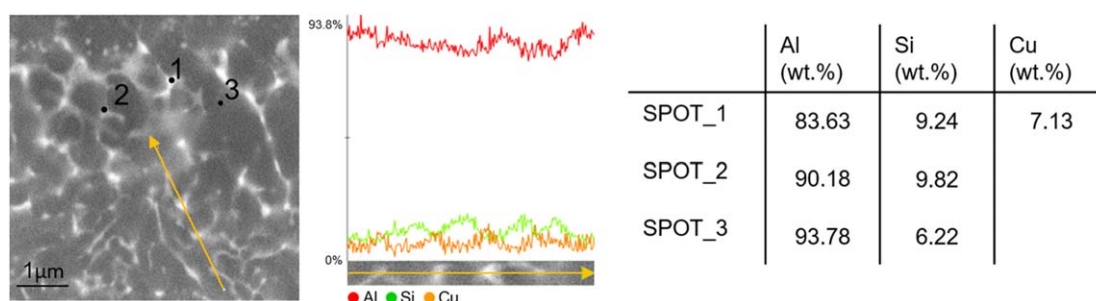


**Figure 9.** EDX analysis performed with a linear scan across the network and with 3 spot scans at different points of the network.

detectors (figure 8) was performed on pre-alloyed AlSi10Cu4Mg samples to investigate the network features. The network appeared to consist of two different phases: one with a higher atomic weight (lighter in the BSE image) and one with a lower atomic weight (darker in the BSE image).

In order to name the lighter and darker phases seen through the FESEM analysis, EDX line and spot investigations were conducted. The EDX results, reported in figure 9, clearly demonstrate how the lighter areas identified with the BSE detector are rich in copper. Looking closer at the linear EDX, it can be seen that when the analysis line intercepts the network in the lighter areas, the concentration of Cu increases and the presence of Si decreases. By performing the point analysis in the lightest part of the network (SPOT\_1), in the darkest part of the network (SPOT\_2) and in the matrix (SPOT\_3), it was stated that copper is predominantly present in the light areas of the network, while in the darker areas the eutectic Al-Si phase is present and in the matrix there is more abundant Al.

In addition, the average cell size in the central zone of the melt pool was calculated obtaining a value of  $0.5 \pm 0.3 \mu\text{m}$  for the pre-alloyed AlSi10Cu4Mg. This average cell size of the pre-alloyed composition was slightly lower than that measured in the mixed AlSi10Mg+4Cu system ( $0.8 \pm 0.4 \mu\text{m}$ ) [23]. This slight variation could be generated by the more homogeneous distribution of  $\text{Al}_2\text{Cu}$  in the AlSi10Cu4Mg composition than in the AlSi10Mg + 4Cu system. It is reasonable to assume that in the mixed AlSi10Mg + 4Cu system the  $\text{Al}_2\text{Cu}$  phase was more abundant in non-homogeneous zones due to the higher presence of Cu. Consequently, in the homogeneous zones considered for the measurements of the cell size, less  $\text{Al}_2\text{Cu}$  phase was present in the network. This distribution could result in a thinner network and, thus, in a slightly higher cell size for the mixed AlSi10Mg + 4Cu system.

Considering the critical role of grain size, morphology and orientation in mechanical behaviour, the EBSD analysis was carried out. From the EBSD map plotted in figure 10, two melt pool zones could be distinguished: a fine zone with equiaxial grains along the melt pool boundaries highlighting a non-preferential orientation and a coarser zone with columnar grains in the melt pool core showing a marked preferred orientation perpendicular to the melt pool boundary and, thus, parallel to the build direction caused by the strong thermal gradient occurring during the PBF-LB/M process. Equiaxial grains are easily distinguishable from columnar grains by their smaller size and aspect ratio close to 1. Evaluating the equivalent circular diameters of equiaxial grains, a



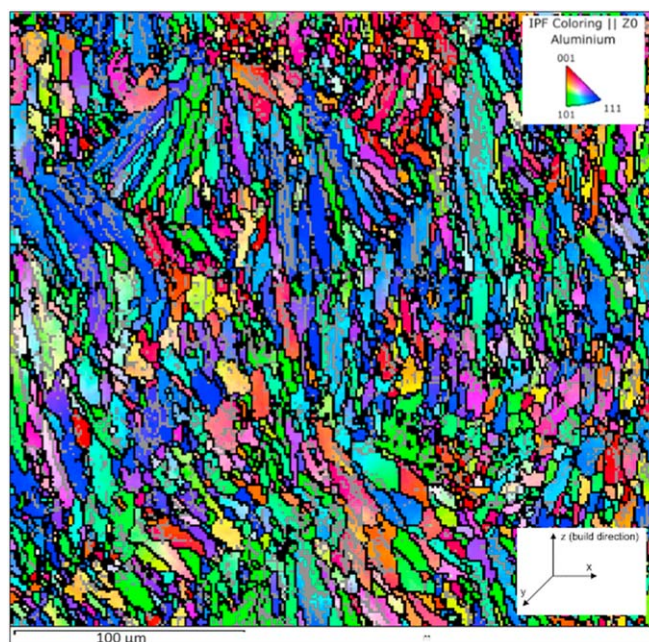


Figure 10. EBSD orientation map taken at 500 X.

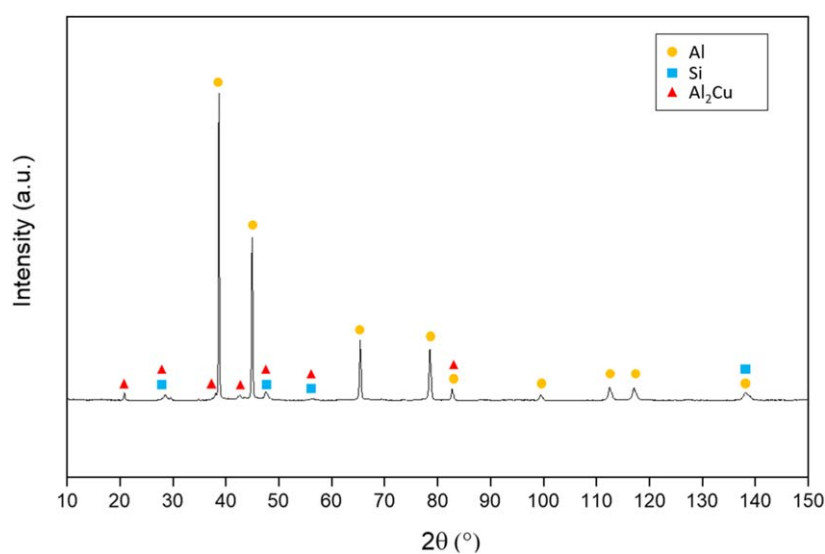


Figure 11. XRD spectrum of the AlSi10Cu4Mg bulk sample on the XZ plane in a  $2\theta$  range of 10–150°.

mean value of  $6.01 \pm 0.82 \mu\text{m}$  was recorded. Comparing this value with the one observed by Bosio *et al* in the mixed AlSi10Mg + 4Cu system ( $7.34 \mu\text{m}$ ) [23], a slight variation could be pointed out.

### 3.4. Assessment of the solid solution and precipitation levels

In order to understand the occurred precipitation and the solid solution level of pre-alloyed AlSi10Cu4Mg composition after PBF-LB/M process, an XRD investigation was conducted (figure 11).

The spectrum displayed in figure 11 revealed the presence of fcc-Al, diamond cubic Si and tetragonal  $\text{Al}_2\text{Cu}$  phase ( $\theta$  phase). A study on the diffusion coefficients of several transition elements in the fcc Al revealed that Cu has one of the highest values [39]. This leads to a higher probability of  $\text{Al}_2\text{Cu}$  precipitation during the rapid solidification. To detect the presence of  $\text{Al}_2\text{Cu}$  phase, a high-resolution EBSD analysis was performed on pre-alloyed AlSi10Cu4Mg samples. By measuring the misorientation between all pixel pairs, in fact, it is possible to identify the boundaries enclosing the individual grains. Putting the phase composition in the Aztec software, the  $\text{Al}_2\text{Cu}$  precipitates were represented on an EBSD map, highlighting their distribution and providing the area

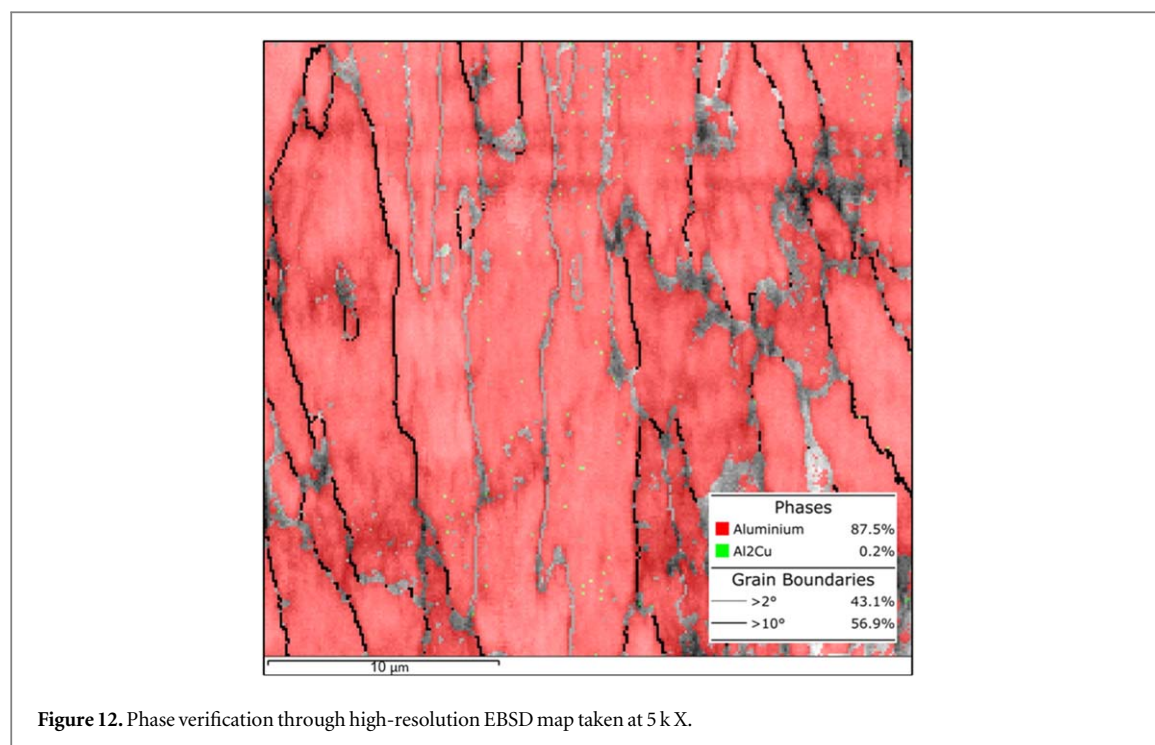


**Figure 12.** Phase verification through high-resolution EBSD map taken at 5 k X.

fraction. The analysis revealed a presence of Al<sub>2</sub>Cu of about 0.2% as area fraction (figure 12). However, it is important to emphasise that the resolution of this type of analysis is around 0.1 μm - 0.02 μm, so nanometric precipitates below 20 nm are difficult to detect. However, the strongly limited percentage of precipitates recorded in AlSi10Cu4Mg samples implies that a large amount of Cu is in solid solution.

To investigate the solid solution condition, XRD data were used to evaluate the fcc-Al lattice parameter. In fact, when solute atoms are present, the alloy lattice is locally distorted, and the lattice parameter results altered. The lattice parameter calculated in pre-alloyed AlSi10Cu4Mg composition was of 0.4041 nm and thus decreased with respect to the pure AlSi10Mg alloy. On the other hand, the lattice parameter measured in the mixed AlSi10Mg+4Cu system was 0.4043 nm. The lower value found in the AlSi10Cu4Mg composition suggests that there are globally more Cu atoms in solid solution in the pre-alloyed system. In fact, the inhomogeneous Cu distribution derived by the mixed powders implied the presence of Cu-rich cluster with a lower Cu atoms number in Al lattice. To support this hypothesis, Vegard's law was used to estimate the saturation level of the alloys. This evaluation in pre-alloyed AlSi10Cu4Mg resulted in a saturation value of Mg, Si and Cu in the Al matrix of about 6.26 at%. Assuming that Mg is entirely in solid solution and Si is in solid solution as in the AlSi10Mg system, the percentage of Cu in solid solution would be equal to 1.9 at%. The value obtained for Cu in the pre-alloyed AlSi10Cu4Mg composition is about twice as high as that recorded in the mixed AlSi10Mg+4Cu system (1 at%). This evidence would seem to confirm the previous considerations on the lattice parameters, i.e. a higher presence of Cu in solid solution in the pre-alloyed AlSi10Cu4Mg.

In order to confirm the different saturation level of AlSi10Cu4Mg and AlSi10Mg+4Cu systems the DSC analysis was considered (figure 13).

The different kinds of reactions occurring in the AlSi10Cu4Mg material during the DSC test can be distinguished based on the peak characteristics, which can be exothermic or endothermic. In particular, nucleation and growth of precipitates is an exothermic reaction that releases energy, whereas the dissolution of precipitates is endothermic and requires energy. The first more intense peak was recorded at 225 °C, and the minor second peak at 340 °C. The enthalpy released in exothermal processes can be measured as the area under the peak, resulting in about 34.5 J g<sup>-1</sup> and 6.4 J g<sup>-1</sup>, respectively for the first and second peaks. According to the exothermic character of the peaks, some precipitation reactions occurred between 178 °C–264 °C and 317 °C–355 °C (as onset and offset values). In particular, according to Riontino *et al* and Edwards *et al*, the exothermic peak recorded at 225 °C could be addressed to the formation of the Al<sub>2</sub>Cu phases in addition to the well-known precipitation of Si [40, 41]. Comparing the DSC results obtained by Marola *et al* on pure AlSi10Mg, the enthalpy released in the first exothermal phenomenon of AlSi10Cu4Mg is 5% higher [42]. The higher enthalpy confirms the contribution of Al<sub>2</sub>Cu phase precipitation in the first peak and, thus, the presence of Cu in the solid solution. On the other hand, the second peak of the DSC spectrum is usually attributed to the Mg<sub>2</sub>Si phase [41]. The peak recorded in the DSC analysis relating to the precipitation of the Mg<sub>2</sub>Si phase together with the absence of the relative peaks in the XRD spectrum, suggests that Mg is completely in solid solution in the as-built condition.

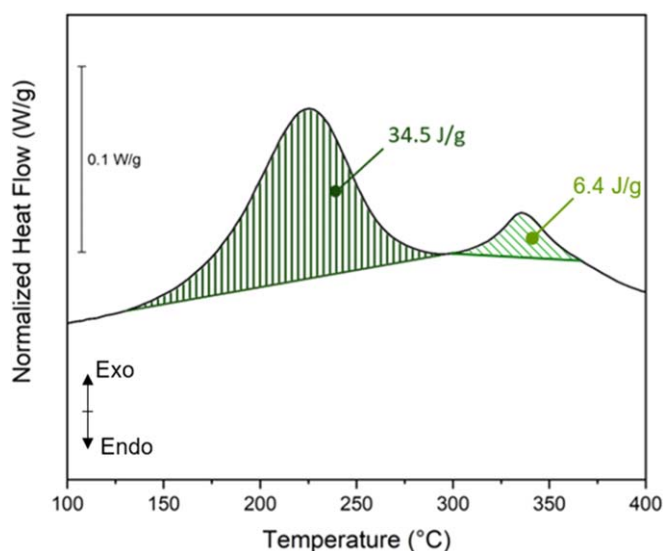


Figure 13. DSC signal of an AlSi10Cu4Mg sample.

By comparing the enthalpy values released in the exothermal phenomenon of  $\text{Al}_2\text{Cu}$  phase precipitation of the pre-alloyed and mixed samples, it is possible to note that the area under the first peak of pre-alloyed AlSi10Cu4Mg was 33% higher than the one measured for mixed AlSi10Mg+4Cu. Assuming the same Si precipitation behaviour in both systems, the higher enthalpy of the first DSC peak related to the pre-alloyed AlSi10Cu4Mg again suggests a more significant presence of Cu in solid solution than in the mixed AlSi10Mg+4Cu.

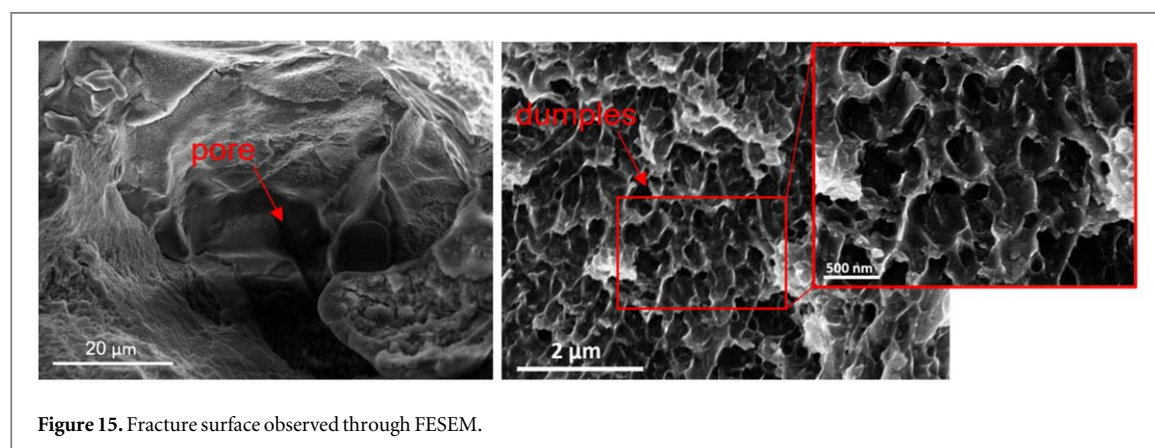
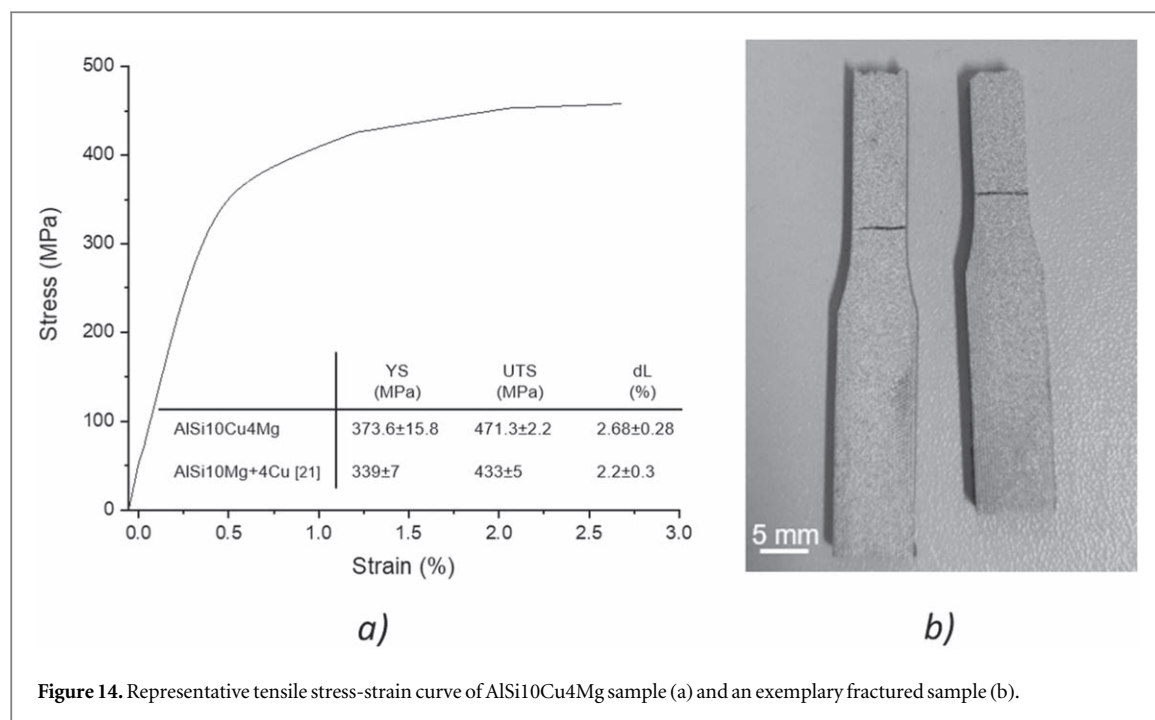
### 3.5. Mechanical properties

To investigate how a higher homogeneous distribution of the alloying elements and a higher percentage of Cu in solid solution can affect the mechanical properties of the pre-alloyed AlSi10Cu4Mg system, microhardness, tensile and compression tests were conducted. As explained in section 3.3, the cell size of the pre-alloyed AlSi10Cu4Mg composition proved to be smaller than the mixed AlSi10Mg+4Cu system. Based on Kempf *et al* evidence, this might suggest a higher hardness of the pre-alloyed AlSi10Cu4Mg system [43]. They have, in fact, observed that there is a direct link between hardness and cell size, and in particular, as the latter decreases, the strength properties increase. Performing microhardness Vickers tests on AlSi10Cu4Mg and averaging ten measurements, a mean microhardness value of about 168 HV was recorded with a standard deviation of approximately 5 HV. This value revealed 18% higher microhardness properties than the mixed AlSi10Mg+4Cu system [23]. This is in accordance with the Kempf *et al* observations and could be explained by the Chen *et al* study conducted on AlSi10Mg. They proved that the Si network at the AlSi10Mg cell boundaries acts as precipitates [44]. The presence of the precipitates does not act merely as a physical obstacle to the dislocation movement but rather as a distortion of the crystal lattice planes in the areas where these precipitates are formed: the localised distortion of the lattice, comparable to localised work hardening, causes the resistance to the dislocation movement and consequently the increase in hardness of the alloy. In the case of the pre-alloyed AlSi10Cu4Mg composition, the smaller cell size resulted in a thickening of the Al-Si-Cu network that acts as precipitates and, thus, leads to an increase in average microhardness values compared to the mixed AlSi10Mg+4Cu system.

As well explained by Ashby *et al*, the microhardness is related by a factor of 1/3 to the yield strength of the material [45]. For this reason, by conducting tensile and compression tests at room temperature on AlSi10Cu4Mg, it is reasonable to expect higher strength values than the mixed AlSi10Mg+4Cu system. A representative tensile curve of the as-built AlSi10Cu4Mg sample with the mechanical values obtained is presented in figure 14(a). On average, the tests exhibited a Young's modulus of  $77.2 \pm 3.1$  GPa, an UTS of  $471.3 \pm 2.2$  MPa, a YS of  $373.6 \pm 15.8$  MPa and  $2.68 \pm 0.28\%$  as the elongation at the break (dL).

Compared to the mixed AlSi10Mg+4Cu system, the AlSi10Cu4Mg showed +10% in both YS and UTS and an elongation at break value more than 20% higher [23, 24]. The significant increase in elongation at break can be reasonably attributed to the absence of brittle Cu clusters in the pre-alloy system that could irreversibly affect the ductility of the alloy. The elongation of the pre-alloyed AlSi10Cu4Mg composition is, in any case, limited when compared to the pure AlSi10Mg system, showing poor ductility. To investigate the reasons for this limited ductility, FESEM analyses were conducted on the fracture surfaces (figure 15).





Observing the fracture surfaces, no cleavage planes typical of brittle fracture were observed, but some porosity detected can be imputed as one of the possible causes of the fracture (figure 15). The presence of a large number of dimples suggested a ductile fracture. Notwithstanding, the low elongation at break, the limited necking of gauge length and the fracture almost perpendicular to the applied load direction would suggest a low-ductile behaviour of the alloy. According to studies conducted on AlSi10Mg, the Al-Si network proved to be a brittle element in fracture mechanics [46, 47]. It is therefore reasonable to assume that this phenomenon could be amplified in the AlSi10Cu4Mg due to the formation of the brittle  $\text{Al}_2\text{Cu}$  phase in the network. In addition, the low-ductile behaviour of the alloy could also be attributed to the residual porosities observed on the AlSi10Cu4Mg fracture surface. The porosities, when subjected to tensile loading, reduce the load capacity of the material by acting as a crack nucleation site. However, residual porosity can be closed with post-processing treatments such as hot isostatic pressing post-processing, thus improving the elongation to the break of pre-alloyed AlSi10Cu4Mg composition [48].

Nevertheless, to better understand the recorded increase in YS and UTS of the pre-alloy AlSi10Cu4Mg system with respect to the mixed AlSi10Mg+4Cu system, it is possible to refer to the three mechanisms that contribute to the YS value of an alloy. According the equation (3):

$$YS = \sigma_{GB} + \sigma_{ss} + \sigma_P \quad (3)$$

where  $\sigma_{GB}$  is the contribution of the grain boundary strengthening mechanism,  $\sigma_{ss}$  the contribution of super-saturated solid solution strengthening mechanism, and  $\sigma_P$  the contribution of precipitation strengthening.

Starting from the  $\sigma_{GB}$  contribution to the alloy YS, it could be calculated through the Hall-Petch equation [45], as follows:

**Table 2.** Overview of the coefficients used to calculate the contribution of solid solution strengthening in the AlSi10Cu4Mg YS.

	$c$ (wt %)	$k$ (MPa/wt % <sup>2/3</sup> )	$\sigma_{ss}$ (MPa)
Mg	0.3	29	17
Si	4.03	66.3	168
Cu	4.33	46.4	123

$$\sigma_{GB} = \sigma_0 + \frac{k}{\sqrt{d}} \quad (4)$$

where  $\sigma_0$  is the friction stress when dislocations glide on the slip plane,  $k$  is the stress concentration factor and  $d$  is the average grain size.

While  $\sigma_0$  and  $k$  were set according to the literature respectively at 10 MPa [49] and 0.4 MPa mm<sup>-2</sup> [50], the average grain size was calculated based on the EBSD analysis reported in section 3.3. Accordingly, a contribution of the grain boundary strengthening mechanism of 15.2 MPa was calculated for the pre-alloyed AlSi10Cu4Mg composition. This value slightly differs from the contribution calculated for the mixed AlSi10Mg+4Cu system (14.7 MPa), but it can not justify the increase in YS recorded in the pre-alloyed composition. Analysing the super-saturated solid solution strengthening, it is reasonable to assume that it significantly contributes to the increase in YS of the pre-alloyed AlSi10Cu4Mg system. In fact, on the basis of the DSC analysis (figure 13) and the lattice parameter calculated from the XRD data, a significantly higher level of solid solution is expected for the pre-alloyed AlSi10Cu4Mg with respect to the mixed AlSi10Mg+4Cu system. To quantify this contribution, the equation based on Myhr *et al* model [51] could be applied, as follows:

$$\sigma_{ss} = \sum k_i c_i^{\frac{2}{3}} \quad (5)$$

where  $k$  is the concentration of  $i$ -solute element in the solid solution and  $c$  is the concentration of  $i$ -alloying element in solid solution.

$k_i$  were fixed based on the Myhr *et al* model, and  $c_i$  were calculated according to Vegard's law applied to the XRD data. In particular, for both systems, it was assumed that the elements in solid solution were mainly Mg, Si and Cu, that Mg was completely in solid solution and that Si was in solid solution similar to the AlSi10Mg system without Cu. The values of  $k$  and  $c$  used are summarised in table 2.

By summing the contributions of the three main elements in solid solution, a  $\sigma_{ss}$  of 308 MPa was obtained for the pre-alloyed AlSi10Cu4Mg samples. A significant increment was observed with respect to the mixed AlSi10Mg+4Cu system where a  $\sigma_{ss}$  of 256 MPa was calculated. It is then reasonable to suppose that the solid solution strengthening has a key role in YS differences recorded between pre-alloyed and mixed systems. Finally,  $\sigma_p$  contribution for the pre-alloyed AlSi10Cu4Mg system was evaluated by the difference between the YS value and the other contributions obtaining a value of 50 MPa. This value slightly differs from the contribution calculated for the mixed AlSi10Mg+4Cu system (69 MPa). This suggests that Cu clusters in the mixed AlSi10Mg+4Cu system acts as dislocation movement inhibitors increasing the  $\sigma_p$  contribution. In this way, the large gap in YS values between the pre-alloyed and mixed compositions can be mainly attributed to the massive increase in  $\sigma_{ss}$  achieved in the pre-alloyed AlSi10Cu4Mg system thanks to high level of Cu solid solution.

The mechanical characterisation of pre-alloyed AlSi10Cu4Mg system was completed with the compressive tests. In figure 16, a representative compressive curve is reported. A mean value of  $375.4 \pm 1.1$  MPa was recorded as Compressive Yield Strength (CYS),  $926.9 \pm 50.7$  MPa as Ultimate Compressive Strength (UCS) and  $22.5 \pm 3.1\%$  as the compression at the break (dL).

While residual porosity could represent a cause of load-capacity reduction when subjected to tensile loading, this may not be a limiting factor when compressive loading is present. The results of the compressive test confirmed this assumption showing a significantly high increment of compressive strength compared with the mixed system of Li *et al* (figure 16) [52]. In particular, if the mixed AlSi10Mg+4Cu system did not exhibit an improvement in CYS with respect to the pure AlSi10Mg system [23, 53], while the pre-alloyed AlSi10Cu4Mg composition allowed an increase of 8%. This result can again be explained by the absence of copper segregations in the AlSi10Cu4Mg, which can embrittle the material until the strengthening resulting from the addition of Cu to the AlSi10Mg system becomes ineffective. In addition, according to tensile results, the compression at break resulted still lower than AlSi10Mg probably due to the embrittlement action of Al<sub>2</sub>Cu [24].

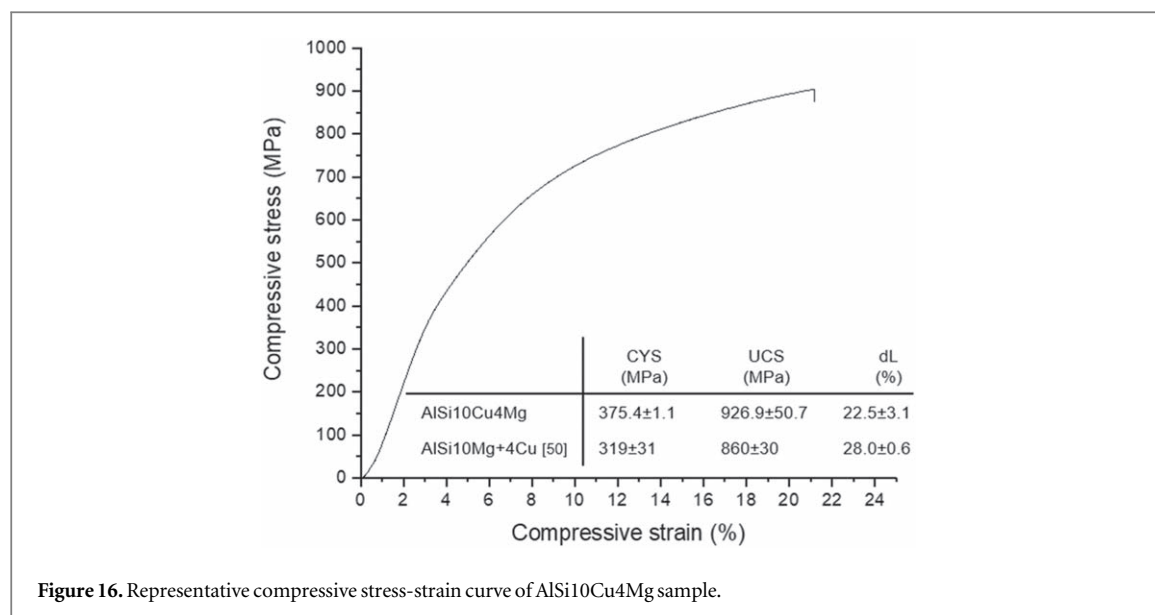


Figure 16. Representative compressive stress-strain curve of AlSi10Cu4Mg sample.

#### 4. Conclusions

A large body of literature demonstrated the benefits of adding 4 wt% Cu to the well-known AlSi10Mg system [22–26]. However, most of the studies on the processability of this composition were carried out on the system obtained from mechanically mixed powders of AlSi10Mg and pure Cu [22–24, 26]. Despite being effortless and cost-saving, this method of obtaining feedstock material based on AlSi10Mg and pure Cu powders leads to significant inhomogeneities of the alloying elements and thus to non-uniform mechanical properties [26]. Gas atomising powders is a powerful way to overcome the problems associated with mechanical mixing. To thoroughly understand the benefits of using pre-alloyed powders on microstructural and mechanical features, an accurate study was conducted on pre-alloyed AlSi10Cu4Mg composition. With the present study the effectiveness of the pre-alloying system in the microstructural and mechanical homogeneity was verified through a comparative study on the mixed system with the same chemical composition. The SST method was used to quickly investigate the laser-powder interaction of the pre-alloyed AlSi10Cu4Mg composition and compare this behaviour with the mixed AlSi10Mg+4Cu system. SST approach was also exploited to select the most suitable P, v and hd values for the bulk samples production. Four parameter combinations were used for the PBF-LB\M production obtaining crack-free and fully dense samples. When process parameters allowing a high densification level were identified, more in-depth microstructural and mechanical characterisations were carried out to compare the peculiarities of AlSi10Cu4Mg and AlSi10Mg+4Cu systems. The results obtained can be summarised as follows:

- Observing of cross-sectioned SSTs and bulk samples revealed any Cu segregation or detrimental defects resulting from an incorrect diffusion of Cu in the pre-alloyed AlSi10Cu4Mg system. These microstructural characterisations preliminarily verified the effectiveness of pre-alloying in Cu homogeneity starting from one and only one laser scan in contrast to the mechanically mixed system.
- The pre-alloyed AlSi10Cu4Mg composition appeared to have a completely homogeneous microstructure with the Al<sub>2</sub>Cu phase integrated in the cellular network, a lower mean cell size ( $0.5 \pm 0.3 \mu\text{m}$ ) and a slightly smaller average size of equiaxial grains ( $6.01 \mu\text{m}$ ) with respect to the mixed AlSi10Mg+4Cu system ( $0.8 \pm 0.4 \mu\text{m}$  and  $7.34 \mu\text{m}$  respectively).
- In pre-alloyed AlSi10Cu4Mg composition the Mg, Si and Cu solid solution percentage was estimated as 6.26 at% with a Cu contribution of 1.9 at% (about twice as much as the mixed system). The higher solid solution level of AlSi10Cu4Mg attested by Vegard's law was then confirmed by DSC analysis, showing a more intense peak related to the Al<sub>2</sub>Cu precipitation.
- Thanks to the higher mean presence of Al<sub>2</sub>Cu in cellular network and the smaller cell sizes, the pre-alloyed AlSi10Cu4Mg composition exhibited a mean microhardness value 18% higher than the mixed AlSi10Mg+4Cu system.
- The tensile test revealed a macroscopically low-ductile fracture (fracture almost perpendicular to the load and limited plastic deformation) but with a typically ductile fracture surface characterised by the presence of

dimples. Overall higher tensile properties were recorded in the pre-alloyed AlSi10Cu4Mg composition compared to the mixed AlSi10Mg+4Cu system (+10% of both YS and UTS).

- Quantifying the three main contributions of the strengthening mechanisms, the increase in YS in the AlSi10Cu4Mg was mainly attributed to the higher level of the solid solution probably due to the higher homogeneity of Cu.
- The AlSi10Cu4Mg showed improved compressive performance than mixed AlSi10Mg+4Cu system.

This study expanded the knowledge of the promising composition AlSi10Cu4Mg demonstrating how a compositionally homogeneous microstructure with higher mechanical properties can be obtained using pre-alloyed powders. By the way, it should be noted that the production of pre-alloyed powders, e.g. through a gas atomisation process, is more expensive than the cost-effective mechanical mixing technique. However, thanks to the homogeneity of the alloying elements obtained with the pre-alloyed AlSi10Cu4Mg system, future heat treatments will not require time- and energy-consuming homogenisation treatments. Furthermore, heat treatments aimed at improving ductility and tailored for this composition should be investigated in the future.

## Acknowledgments

A special acknowledgement goes to Enrico Virgillito, who contributed to the powder gas atomisation.

## Data availability statement

All data that support the findings of this study are included within the article (and any supplementary files).

## ORCID iDs

A Martucci  <https://orcid.org/0000-0003-1093-8273>

## References

- [1] Frazier W E 2014 Metal additive manufacturing: a review *J. Mater. Eng. Perform.* **23** 1917–28
- [2] Gu D D, Meiners W, Wissenbach K and Poprawe R 2012 Laser additive manufacturing of metallic components: Materials, processes and mechanisms *Int. Mater. Rev.* **57** 133–64
- [3] Lee H, Lim C H J, Low M J, Tham N, Murukeshan V M and Kim Y J 2017 Lasers in additive manufacturing: a review *Int. J. Precis. Eng. Manuf. - Green Technol.* **4** 307–22
- [4] Scipioni Bertoli U, Guss G, Wu S, Matthews M J and Schoenung J M 2017 *In-situ* characterization of laser-powder interaction and cooling rates through high-speed imaging of powder bed fusion additive manufacturing *Mater. Des.* **135** 385–96
- [5] Khairallah S A, Anderson A T, Rubenchik A and King W E 2016 Laser powder-bed fusion additive manufacturing: physics of complex melt flow and formation mechanisms of pores, spatter, and denudation zones *Acta Mater.* **108** 36–45
- [6] Olakanmi E O, Cochrane R F and Dalgarno K W 2015 A review on selective laser sintering/melting (SLS/SLM) of aluminium alloy powders: processing, microstructure, and properties *Prog. Mater. Sci.* **74** 401–77
- [7] Aversa A et al 2019 New aluminum alloys specifically designed for laser powder bed fusion: a review *Materials (Basel)* **12** 1007
- [8] Wang Z et al 2020 Selective laser melting of aluminum and its alloys *Materials (Basel)* **13** 1–67
- [9] Knoop D, Lutz A, Mais B and von Hehl A 2020 A tailored AlSiMg alloy for laser powder bed fusion *Metals (Basel)* **10** 1–13
- [10] Aota L S, Bajaj P, Sandim H R Z and Jägle E A 2020 Laser powder-bed fusion as an alloy development tool: parameter selection for *in situ* alloying using elemental powders *Materials* **13** 3822
- [11] Hornbogen E 2001 Hundred Years of Precipitation Hardening *Journal of Light Metals* **1** 127–32
- [12] Andrade B H S et al 2022 Influence of strain rate on mechanical properties of a CuAlMnTiB shape memory alloy *J. Mater. Res. Technol.* **16** 1667–72
- [13] Silva D D S et al 2022 Effects of long-term thermal cycling on martensitic transformation temperatures and thermodynamic parameters of polycrystalline CuAlBeCr shape memory alloy *J. Therm. Anal. Calorim.* **147** 7875–81
- [14] Karg M, Ahuja B, Kuryntsev S, Gorunov A and Schmidt M 2014 Processability of high strength aluminium-copper alloys AW-2022 and 2024 by laser beam melting in powder bed *25th Annu. Int. Solid Free. Fabr. Symp. An Addit. Manuf. Conf. SFF* **2014** 420–36
- [15] Ahuja B, Karg M, Nagulin K Y and Schmidt M 2014 Fabrication and characterization of high strength Al-Cu alloys processed using laser beam melting in metal powder bed *Phys. Procedia* **56** 135–46
- [16] Muller K 2021 Solidification Cracking in Binary Al-Cu Alloys Additively Manufactured through Laser Powder Bed Fusion *Electronic Theses and Dissertations* **736** (<https://stars.library.ucf.edu/etd2020/736>)
- [17] Zhang H, Zhu H, Qi T, Hu Z and Zeng X 2016 Selective laser melting of high strength Al-Cu-Mg alloys: Processing, microstructure and mechanical properties *Mater. Sci. Eng. A* **656** 47–54
- [18] Nie X, Zhang H, Zhu H, Hu Z, Ke L and Zeng X 2018 Analysis of processing parameters and characteristics of selective laser melted high strength Al-Cu-Mg alloys: From single tracks to cubic samples *J. Mater. Process. Technol.* **256** 69–77
- [19] Marioara C D et al 2007 The effect of Cu on precipitation in Al—Mg—Si alloys 6435 *Philosophical Magazine* **87** 3385–413
- [20] Ding L et al 2018 The structural and compositional evolution of precipitates in Al-Mg-Si-Cu alloy *Acta Mater.* **145** 437–50



- [21] Garmendia X, Chalker S, Bilton M, Sutcliffe C J and Chalker P R 2020 Microstructure and mechanical properties of Cu-modified AlSi10Mg fabricated by laser-powder bed Fusion *Materialia* **9** 100590
- [22] Marola S et al 2020 Alloying AlSi10Mg and Cu powders in laser single scan tracks, melt spinning, and laser powder bed fusion *J. Alloys Compd.* **821** 153538
- [23] Bosio F, Fino P, Manfredi D and Lombardi M 2021 Strengthening strategies for an Al alloy processed by *in situ* alloying during laser powder bed fusion *Mater. Des.* **212** 110247
- [24] Li G, Huang X, Wei H, Liu T and Vanmeensel K 2020 Laser powder bed fusion of a novel Cu-modified AlSi10Mg alloy : processing, microstructure, and properties *Euro PM2020 Virtual Congr.* 1–6
- [25] Martin A et al 2021 Effect of the heat treatment on the microstructure and hardness evolution of a AlSi10MgCu alloy designed for laser powder bed fusion *Mater. Sci. Eng.A* **819** 141487
- [26] Bosio F, Manfredi D and Lombardi M 2022 Homogenization of an Al alloy processed by laser powder bed fusion *in situ* alloying *J. Alloys Compd.* **904** 164079
- [27] Stopyra W, Gruber K, Smolina I, Kurzynowski T and Kuźnicka B 2020 Laser powder bed fusion of AA7075 alloy: influence of process parameters on porosity and hot cracking *Addit. Manuf.* **35** 2019
- [28] Aversa A et al 2018 Single scan track analyses on aluminium based powders *J. Mater. Process. Technol.* **255** 17–25
- [29] Martucci A et al 2021 An automatic on top analysis of single scan tracks to evaluate the laser powder bed fusion building parameters *Materials* **14** 5171
- [30] Bosio F et al 2019 A time-saving and cost-effective method to process alloys by Laser Powder Bed Fusion *Mater. Des.* **181** 107949
- [31] Butler C, Babu S, Lundy R, O'Reilly Meehan R, Punch J and Jeffers N 2021 Effects of processing parameters and heat treatment on thermal conductivity of additively manufactured AlSi10Mg by selective laser melting *Mater. Charact.* **173** 110945
- [32] Kou S 2021 Predicting susceptibility to solidification cracking and liquation cracking by calphad *Metals* **11** 1442
- [33] Samuel A M, Gauthier J and Samuel F H 1996 Microstructural aspects of the dissolution and melting of Al<sub>2</sub>Cu phase in Al-Si alloys during solution heat treatment *Metall. Mater. Trans. A Phys. Metall. Mater. Sci.* **27** 1785–98
- [34] Weingarten C, Buchbinder D, Pirch N, Meiners W, Wissenbach K and Poprawe R 2015 Formation and reduction of hydrogen porosity during selective laser melting of AlSi10Mg *J. Mater. Process. Technol.* **221** 112–20
- [35] Aboulkhair N T, Everitt N M, Ashcroft I and Tuck C 2014 Reducing porosity in AlSi10Mg parts processed by selective laser melting *Addit. Manuf.* **1** 77–86
- [36] Thijs L, Kempen K, Kruth J P and Van Humbeeck J 2013 Fine-structured aluminium products with controllable texture by selective laser melting of pre-alloyed AlSi10Mg powder *Acta Mater.* **61** 1809–19
- [37] Mertens A, Delahaye J, Dedry O, Vertruyen B, Tchuindjang J T and Habraken A M 2020 Microstructure and properties of SLM AlSi10Mg: Understanding the influence of the local thermal history *Procedia Manuf.* **47** 1089–95
- [38] Cao Y et al 2021 Microstructure evolution and mechanical properties at high temperature of selective laser melted AlSi10Mg *J. Mater. Sci. Technol.* **62** 162–72
- [39] Du Y et al 2003 Diffusion coefficients of some solutes in fcc and liquid Al: Critical evaluation and correlation *Mater. Sci. Eng.A* **363** 140–51
- [40] Riontino G and Zanada A 1998 Coupled formation of hardening particles on pre-precipitates in an Al-Cu-Mg-Si 2014 alloy *Mater. Lett.* **37** 241–5
- [41] Edwards G A, Stiller K, Dunlop G L and Couper M J 1998 The precipitation sequence in Al-Mg-Si alloys *Acta Mater.* **46** 3893–904
- [42] Marola S et al 2018 A comparison of selective laser melting with bulk rapid solidification of AlSi10Mg alloy *J. Alloys Compd.* **742** 271–9
- [43] Kempf A and Hilgenberg K 2020 Influence of sub-cell structure on the mechanical properties of AlSi10Mg manufactured by laser powder bed fusion *Mater. Sci. Eng.A* **776** 138976
- [44] Chen B et al 2017 Strength and strain hardening of a selective laser melted AlSi10Mg alloy *Scr. Mater.* **141** 45–9
- [45] Ashby M, Shercliff H and Cebon D 2018 Materials: Engineering, Science, Processing and Design
- [46] Yan C, Hao L, Hussein A, Bubbs S L, Young P and Raymont D 2014 Evaluation of light-weight AlSi10Mg periodic cellular lattice structures fabricated via direct metal laser sintering *J. Mater. Process. Technol.* **214** 856–64
- [47] Hitzler L et al 2017 Direction and location dependency of selective laser melted AlSi10Mg specimens *J. Mater. Process. Technol.* **243** 48–61
- [48] Liu X, Liu Y, Zhou Z, Zhong H and Zhan Q 2022 A combination strategy for additive manufacturing of AA2024 high-strength aluminium alloys fabricated by laser powder bed fusion: Role of hot isostatic pressing *Mater. Sci. Eng.* **850** 143597
- [49] Yang K V, Rometsch P, Davies C H J, Huang A and Wu X 2018 Effect of heat treatment on the microstructure and anisotropy in mechanical properties of A357 alloy produced by selective laser melting *Mater. Des.* **154** 275–90
- [50] Starink M J, Cao L F and Rometsch P A 2012 A model for the thermodynamics of and strengthening due to co-clusters in Al-Mg-Si-based alloys *Acta Mater.* **60** 4194–207
- [51] Myhr O R, Grong O and Andersen S J 2001 Modelling of the age hardening behaviour of Al-Mg-Si alloys *Acta Mater.* **49** 65–75
- [52] Li G, Huang X, Wei H, Liu T and Vanmeensel K 2020 Laser powder bed fusion of a novel Cu-modified AlSi10Mg alloy: processing, microstructure, and properties *Proc. - Euro PM2020 Congr. Exhib., no*
- [53] Sert E, Hitzler L, Hafenstein S, Merkel M, Werner E and Öchsner A 2020 Tensile and compressive behaviour of additively manufactured AlSi10Mg samples *Prog. Addit. Manuf.* **5** 305–13